Article

Understanding Composition-Dependent Synergy of PtPd Alloy Nanoparticles in Electrocatalytic Oxygen Reduction Reaction

Jinfang Wu,[†,‡] Shiyao Shan,[‡] Hannah Cronk,[‡] Fangfang Chang,[‡] Haval Kareem,[‡] Yinguang Zhao,[‡] Jin Luo,[‡] Valeri Petkov,[*,§] and Chuan-Jian Zhong[*,‡]

[†]Department of Chemistry and Chemical Engineering, Inner Mongolia University, Hohhot 010021, China
[‡]Department of Chemistry, State University of New York at Binghamton, Binghamton, New York 13902, United States
[§]Department of Physics, Central Michigan University, Mount Pleasant, Michigan 48859, United States

Ⓢ Supporting Information

ABSTRACT: Gaining an insight into the relationship between the bimetallic composition and catalytic activity is essential for the design of nanoalloy catalysts for oxygen reduction reaction. This report describes findings of a study of the composition−activity relationship for PtPd nanoalloy catalysts in oxygen reduction reaction (ORR). Pt_nPd_{100-n} nanoalloys with different bimetallic compositions are synthesized by wet chemical method. While the size of the $Pt_{50}Pd_{50}$ nanoparticles is the largest among the nanoparticles with different compositions, the characterization of the nanoalloys using synchrotron high-energy X-ray diffraction (HE-XRD) coupled to atomic pair distribution function (PDF) analysis reveals that the nanoalloy with an atomic Pt:Pd ratio of 50:50 exhibits an intermediate lattice parameter. Electrochemical characterization of the nanoalloys shows a minimum ORR activity at Pt:Pd ratio close to 50:50, whereas a maximum activity is achieved at Pt:Pd ratio close to 10:90. The composition−activity correlation is assessed by theoretical modeling based on DFT calculation of nanoalloy clusters. In addition to showing an electron transfer from PtPd alloy to oxygen upon its adsorption on the nanoalloy, a relatively large energy difference between HOMO for nanoalloy and LUMO for oxygen is revealed for the nanoalloy with an atomic Pt:Pd ratio of 50:50. By analysis of the adsorption of OH species on PtPd (111) surfaces of different compositions, the strongest adsorption energy is observed for $Pt_{96}Pd_{105}$ (Pt:Pd $\approx$ 50:50) cluster, which is believed to be likely responsible for the reduced activity. Interestingly, the adsorption energy on $Pt_{24}Pd_{177}$ (Pt:Pd $\approx$ 10:90) cluster falls in between $Pt_{96}Pd_{105}$ and Pd_{201} clusters, which is believed to be linked to the observation of the highest catalytic activity for the nanoalloy with an atomic Pt:Pd ratio of 10:90. These findings have implications for the design of composition-tunable nanoalloy catalysts for ORR.
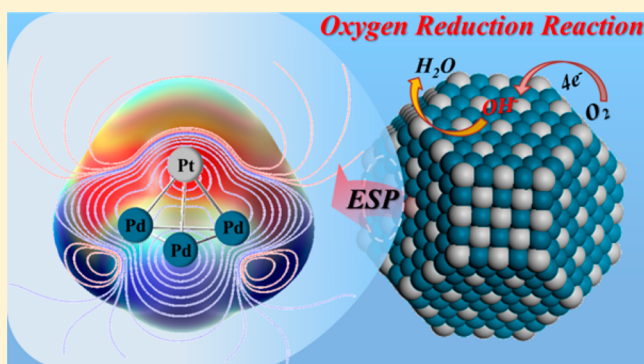
1. INTRODUCTION

Pt is currently a choice of catalysts for the cathode reaction in a proton exchange membrane fuel cell (PEMFC). However, the high cost of Pt is one of the bottlenecks for the ultimate commercialization of PEMFCs. The development of electrocatalysts of Pt alloyed with different transition metals has been an important pathway toward decreasing Pt loading in the catalysts for oxygen reduction reaction (ORR), including transition metals such as Ni, Co, Cu, Fe, Pd, Ag, etc.[1−8] Among them, the study of PtPd for ORR is particularly remarkable. One important focus is alloying Pt and Pd atoms to form nanoparticle alloy catalysts. For example, two kinds of PtPd supported on carbon were prepared by coimpregnation and sequential impregnation of Pt on Pd/C [Pt(Pd/C)] for ORR.[9] While both showed lower ORR activities than Pt/C, they showed largely enhanced activity compared to Pd/C. The catalytic activity of PtPd nanoparticles is related to the composition. A previous study of the influence of Pt: Pd

atomic ratios (1:2−1:8) on ORR activity showed that decreasing the atomic ratio of Pt:Pd led to an increase in the particle size with decreased electrochemical surface area (ECA) and electrocatalytic activity, in which a maximum activity of ORR was revealed at an atomic ratio of Pt: Pd = 1:2.[10] A recent theoretical study of the composition-dependent thermal stability of PtPd clusters with 55 atoms found that $Pd_{43}Pt_{12}$ exhibits the highest stability due to its weakest O_2 adsorption strength compared to the Pt_{55}, Pd_{55}, and $Pd_{13}Pt_{42}$ clusters, indicating good catalytic activities toward ORR.[11] PtPd/C catalysts prepared by polyol process in ethylene glycol solution showed that the catalytic activity of Pt_3Pd_1/C for ORR is improved compared with Pt/C or Pt_1Pd_1/C catalyst.[12] On the other hand, PtPd alloy with particular shapes, such as hollow

nanocages, nanocubes, nanoporous, polyhedron and core−shell structures, is another focus of the recent studies.[13−19] For example, the PtPd nanocages prepared by potential cycling treatment showed superior catalytic activity and good structural stability toward ORR in comparison with core−shell Pd@Pt nanodendrites and commercial Pt catalysts.[20]

Despite the previous studies showing the preparation of PtPd catalysts toward enhanced catalytic activities, the question of how the catalytic activity is correlated with the atomic-scale structure and bimetallic composition in the nanoparticles remains elusive. Recently, our studies of PdNi and PdCu nanoalloys revealed an intriguing composition-activity correlation for ORR with the help of high-energy X-ray diffraction (XRD) coupled to atomic pair distribution function (PDF) analysis[21] and DFT calculation.[22] The understanding of how this type of structural correlation operates for PtPd nanoalloys could provide further information for assessing the general structure-catalytic synergy of the bimetallic nanoalloy catalysts. This paper mainly focuses on the study of composition-activity correlation for PtPd nanoalloys in ORR, the understanding of which is aided by DFT calculations of cluster models involving the adsorption of OH and oxygen species in the process of ORR.

2. EXPERIMENTAL SECTION

2.1. Chemicals. Platinum(II) acetylacetonate (Pt (acac)$_2$, 97%), palladium(II) acetylacetonate (Pd(acac)$_2$, 97%), dioctyl ether ([CH$_3$(CH$_2$)$_7$]$_2$O, 99%), oleylamine (CH$_3$(CH$_2$)$_7$CH CH(CH$_2$)$_8$NH$_2$, 70%), oleic acid (CH$_3$(CH$_2$)$_7$CH CH-(CH$_2$)$_7$COOH, 99+%), and 1,2-hexadecanediol (90%) came from Aldrich. Other chemicals including ethanol, hexane, and potassium choloride were purchased from Fisher Scientific. Vulcan carbon XC-72 was from Cabot. All gases were obtained from Airgas.

2.2. PtPd Nanoalloy Synthesis and Catalyst Preparation. Pt$_n$Pd$_{100-n}$ alloy nanoparticles (NPs) (n represents atomic percentage of Pt in the NPs) were synthesized following the protocol. First, Pt(acac)$_2$ and Pd(acac)$_2$ as metal precursors were mixed into dioctyl ether solvent following a controlled molar ratio; meanwhile, the capping agents involving oleic acid and oleylamine were also added into the solvent, as well as 1,2-hexadecanediol as the reducing agent. Sequentially, the solution was heated gradually to 220 °C with reflux for 30 min under N$_2$ atmosphere. Finally, the solution was cooled back to room temperature, followed by precipitating out of the resulting PtPd NPs by washing and centrifugation. Details for the synthesis are included in Supporting Information.

The preparation of PtPd catalysts involved the assembly of PtPd NPs on the carbon support hereafter referred as PtPd/C, and then its activation. In assembly process, a controlled amount of PtPd NPs and carbon (XC-72) were adequately mixed in hexane solution through sonication and overnight stirring. The resulting PtPd/C NPs were then dried under N$_2$ atmosphere. The activation of PtPd/C NPs was performed by thermochemical treatment.[21,23,24] Briefly, PtPd/C NPs were first kept at 260 °C under N$_2$ atmosphere for 0.5 h to remove the organic capping molecules on the NP surface, and further treated at 400 °C under 15% H$_2$ − 85% N$_2$ atmosphere for 2 h for calcination in a programmable furnace. The weight loadings on the carbon support were 30% for Pt$_{14}$Pd$_{86}$/C, 14% for Pt$_{47}$Pd$_{53}$/C, and 24% for Pt$_{64}$Pd$_{36}$/C, as determined by thermogravimetric analysis (TGA) performed on a PerkinElmer Pyris 1-TGA. It is important to note that the preparatory

feeding values in supporting the PtPd NPs on carbon were the same for all samples. The differences in the final metal loading after the thermochemical treatment were due to a subtle difference in carbon burning among these catalysts which occurred during the thermochemical treatment. Note also that these differences did not affect the assessments of the catalytic activities since the measured currents were normalized against the total metal mass.

2.3. Morphology, Composition and Structural Characterization. The chemical composition of the PtPd NPs was analyzed by inductively coupled plasma−optical emission spectroscopy (ICP−OES). It was performed on a PerkinElmer 2000 DV ICP−OES instrument using a Meinhardt nebulizer coupled to a cyclonic spray chamber with the following parameters: 18.0 L of Ar(g)/min for plasma; 0.63 L of Ar(g)/ min for nebulizer; 0.3 L of Ar(g)/min for auxiliary; 1500 W for the power; 1.00 mL/min for peristaltic pump rate. After every 6 or 12 samples, laboratory check standards were analyzed to make the standards be within ±5% of the initial concentration.

High-angle annular dark-field scanning TEM (HAADF-STEM) was employed to determine the morphology of the PtPd/C catalysts on a JEOL JEM 2100F instrument equipped with a CEOS hexapole probe. The instrument was operated at 200 keV in STEM mode. The lens settings combined with the corrector tuning gave a spatial resolution of ∼90 pm. High-resolution TEM (HRTEM) measurements were performed on a JEOL JEM 2010F with an acceleration voltage of 200 kV and a routine point-to-point resolution of 0.194 nm. During the measurements, the hexane suspension of the PtPd NPs as samples was dropped onto a carbon-coated copper grid followed by solvent evaporation at room temperature.

X-ray photoelectron spectroscopy (XPS) measurements were performed following a protocol reported previously.[24] The measurements were done on a Kratos AXIS Ultra DLD spectrometer using monochromatic Al source. The spectrometer was calibrated with respect to the Au 4f$_{7/2}$ (84.0 eV) and Cu 2p$_{3/2}$ (932.7 eV) lines. The pass energy was fixed at 20 eV for the detailed scans. The percentages of near-surface Au and Pd species in the NPs were determined by analyzing the areas of the respective XPS peaks.

Synchrotron high-energy XRD (HE-XRD) with atomic pair distribution functions (PDFs) measurements were performed in *ex situ* mode using X-ray (wavelength, λ = 0.1080 Å) at Sector 11 of the Advanced Photon Source, Argonne National Laboratory. HE-XRD patterns of PtPd/C samples were reduced to the structure factors, $S(q)$, and further to atomic PDFs, $G(r)$ by Fourier transformation. Note that $G(r)$ represents experimental quantities that oscillate around zero and shows positive peaks at real space distances, r, where the local atomic density $\rho(r)$ exceeds the average one ρ_o. By definition, $G(r) = 4\pi r \rho_o [\rho(r)/\rho_o − 1]$, where $\rho(r)$ and ρ_o are the local and average atomic number density, respectively. It is pretty efficient to study the atomic-scale structure of nanosized materials, including metallic alloy NPs by using high-energy XRD and atomic PDFs.[25−27]

2.4. Electrochemical Measurements. Cyclic voltammetry (CV) and rotating disk electrode (RDE) measurements were performed in three-electrode electrochemical cells with a Pt wire as the counter electrode and Ag/AgCl (KCl sat.) as the reference electrode on a computer controlled electrochemical analyzer (CHI600a, CH Instruments) at room temperature. Glassy carbon disk (geometric area, 0.196 cm^2; polished with 0.05 μm Al$_2$O$_3$ powders) coated with a layer of PtPd/C

catalysts was the working electrode. To prepare the working electrode, a typical suspension of the catalysts was prepared by adding 5 mg catalyst (PtPd/C) to 5 mL of 0.25 wt% Nafion solution, followed by ultrasonication for 10 min. Then 10 μL of the suspension was quantitatively dropped to the surface of the polished GC disk and dried under a lamp. The electrolytic solution (0.1 M $HClO_4$) was deaerated with N_2 before the CV measurements, or saturated with oxygen for RDE measurements. Before CV and RDE measurements, the samples underwent 10 potential cycles between 0.02 and 1.2 V (vs RHE) in N_2-saturated 0.1 M $HClO_4$ solution at 50 mV/s to remove possible surface contaminants.

2.5. Computational Modeling. Density functional theory (DFT) calculations are carried out in DMol3 program of Materials Studio suite (Accelrys Inc.) and Gaussian 09 software. First, a small while realistic, Pt_xPd_{4-x} (x = 0, 1, 2, 3, 4) clusters were used to investigate electronic properties and molecular orbital analysis of PtPd catalyst through Gaussian 09 software by B3LYP functional with LanL2DZ basis set. The structures were relaxed without imposing any symmetry constraints and vibrational frequencies were calculated to verify that the optimized structures were at energy mimimum.[28-30] Then, building the adsorption configuration of O_2 on PtPd clusters using Materials Studios, and simulating its parameters by Dmol3.[31-36] In order to be closer to the realistic condition, herein a tetrakaidecahedron model of Pd_xPt_{201-x} (x = 201, 144, 105, 57, 0) cluster including solvation was used. In the calculations, the generalized gradient approximation (GGA) with Perdew−Burke−Ernzerh (PBE) exchange correlation functional was used. The localized double numerical basis sets with polarization functions (DNP) was employed for the valence orbitals, and DFT semicore pseudopots employed to freeze the core electrons of metallic species. The interactions between the model atomic configurations and OH or O_2 molecule were explored. The adsorption energy of OH and O_2 on the model atomic configurations was used as a measure of the adsorption strength. It was calculated by $E_{ads} = -(E_{O_2-metal} - E_{metal} - E_{O_2})$, where, $E_{O_2-metal}$, E_{metal}, and E_{O_2} are total energy for the O_2−metal complex, the isolated metal cluster and the isolated O_2 molecule, respectively. Figure 1 illustrates the four-atom and tetrakaidecahedron models of Pd clusters used in this work.
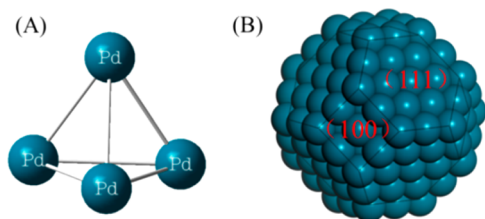

Figure 1. Schematic illustrations of four-atom model of Pd4 cluster (A) and tetrakaidecahedron model of Pd201 (B) clusters.

3. RESULTS AND DISCUSSION

3.1. Composition and Morphology of PtPd Nanoparticles. The composition of as-synthesized Pt_nPd_{100-n} nanoparticles was analyzed by ICP−OES to determine the controllability of the synthesis protocol with respect to the bimetallic composition. Figure 2 shows the composition of as-synthesized Pt_nPd_{100-n} (n = 14, 47 and 64) nanoparticles vs the
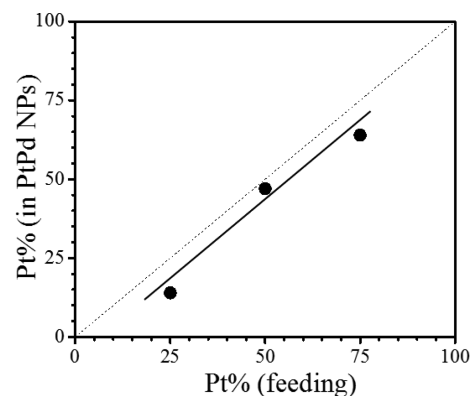

Figure 2. Plot of Pt atomic composition in Pt_nPd_{100-n} nanoparticles (from ICP−OES analysis) vs the synthetic feeding composition. The dashed line represents a 1:1 relationship. The solid line represents the linear fitting to the NPs/C data (slope = 1; R^2 = 0.934).

synthetic feeding ratio (also see Table S1, Supporting Information). The close 1-to-1 relationship of Pt % in as-synthesized PtPd NPs vs the feeding Pt % demonstrates that the composition of the binary alloy PtPd NPs can be controlled well by controlling the feeding ratio of the metal precursors in the synthesis.

The nanoparticles were supported on carbon using the protocol reported previously.[21] The sizes of the carbon-supported nanoparticles, Pt_nPd_{100-n}/C NPs, are 4.7 ± 0.5, 5.6 ± 1.0, and 4.1 ± 0.6 nm for n = 14, 47, and 64, respectively. Figure 3 shows an example for the $Pt_{47}Pd_{53}$ nanoparticles. High
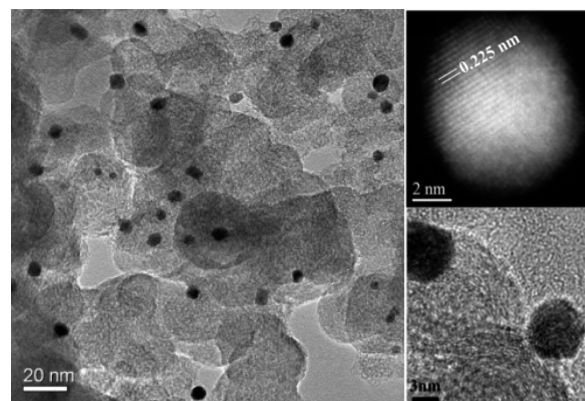

Figure 3. TEM (left panel) and high-angle annular dark field scanning TEM (upper panel) and high-resolution TEM (lower panel) for $Pt_{47}Pd_{53}$/C nanoparticles.

resolution analysis of the lattice fringe yields a value of ~0.225 nm, which is characteristic of (111) facets on the nanoparticles. Similar lattice fringes have also been observed for PtPd nanoparticles of the other compositions. TEM images of the other samples are shown in Figure S2 in Supporting Information.

The nanoparticles were examined using high angle annular dark field (HAADF) scanning transmission electron microscopy (STEM) and energy dispersive spectroscopy (EDS), which provided further information for analyzing the detailed morphology and elemental distribution of Pt and Pd atoms in the Pt_nPd_{100-n} (n = 14, 47, and 64) NPs. A representative set of HAADF-STEM images (top panel) and elemental EDS maps (bottom panel) is shown in Figure 4.
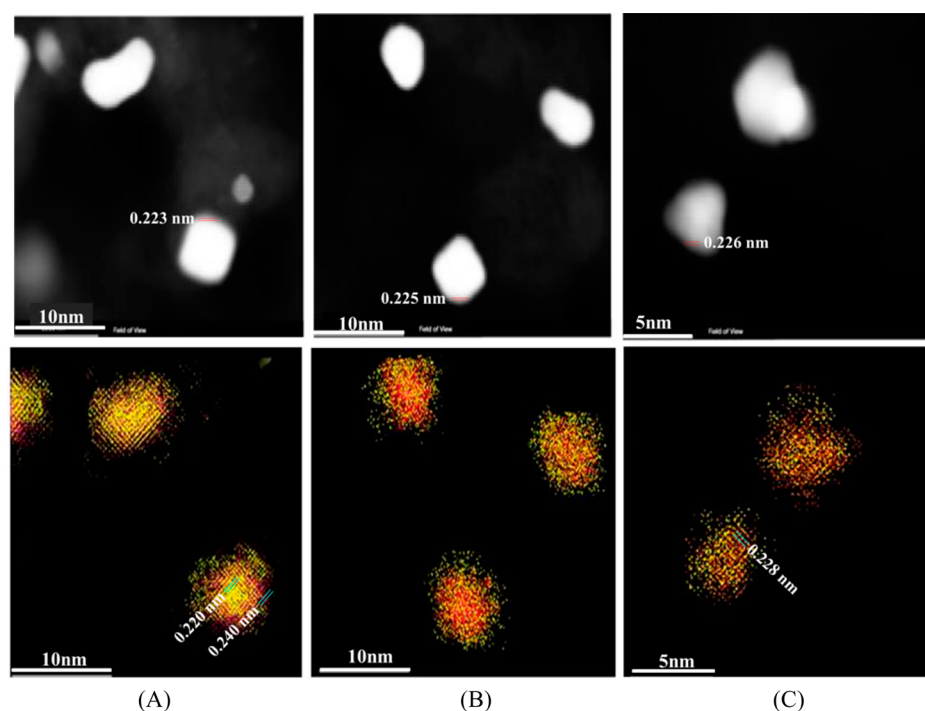
Figure 4. High-angle annular dark field scanning HAADF-STEM images (top panel) and elemental EDS maps of Pt and Pd for Pt_nPd_{100-n} ($n = 14$ (A), 47 (B), and 64 (C)) nanoparticles (Pt species are in red and Pd species are in yellow) .
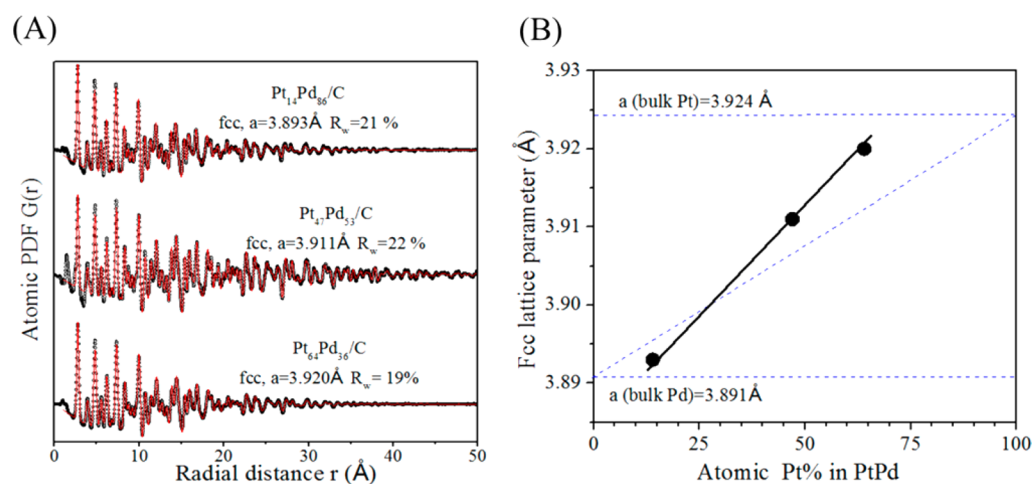

Figure 5. (A) Experimental (symbols) and model-derived (lines) atomic PDFs for carbon supported Pt_nPd_{100-n} ($n = 14$, 47 and 64) nanoparticles thermal-treated under $N_2 + H_2$; Lines in red represent the best model approximation to the experimental data. (B) Plot of the fcc-lattice parameters as a function of relative Pt content in the nanoparticles.

The results show that the PtPd NPs are crystalline, especially for Pt_nPd_{100-n} ($n = 14$, 47, and 64) NPs. Pt and Pd species appear to distribute uniformly across the NPs. This is consistent with the random alloy characteristic of the PtPd NPs with different compositions. In addition, the values of lattice fringes (top panel of Figure 4) are characteristic of (111) facets on the nanoparticles. The lattice constants increase with increasing the atomic ratio of Pt in the nanoparticles. From the elemental mapping images (see bottom panel of Figure 4), the orientation of Pt (red) and Pd (yellow) in the alloyed crystal planes can be clearly identified for $Pt_{14}Pd_{86}$ and $Pt_{64}Pd_{36}$. For $Pt_{14}Pd_{86}$, the alloying appear to increase the lattice for Pt (~0.240 nm) and decrease for Pd (~0.220 nm), respectively. While the lattice constants for Pt and Pd atoms were kept almost same (~0.228 nm), showing overlap of their crystal

planes, there was an apparent disorder for the arrangement of Pt and Pd atoms in $Pt_{47}Pd_{53}$, making it hard to distinguish their respective lattice fringes. These composition-dependent lattice shrinking and atomic disordering characteristics are believed to be related to the structural correlation of their catalytic activities, as discussed in the next subsections.

3.2. Lattice Parameters of PtPd/C Catalysts. The alloying structures of PtPd catalysts were examined by HE-XRD/PDF. A representative set of atomic PDFs extracted from HE-XRD patterns is shown in Figure 5A for the thermochemically treated PtPd nanoparticles with different compositions. The thermal treatment was performed under N_2 at 260 °C followed by H_2 at 400 °C. The three compositions of Pt_nPd_{100-n} ($n = 14$, 47 and 64) all feature an fcc-type structure. The changes of fcc-lattice parameters are shown in Figure 5B. It is
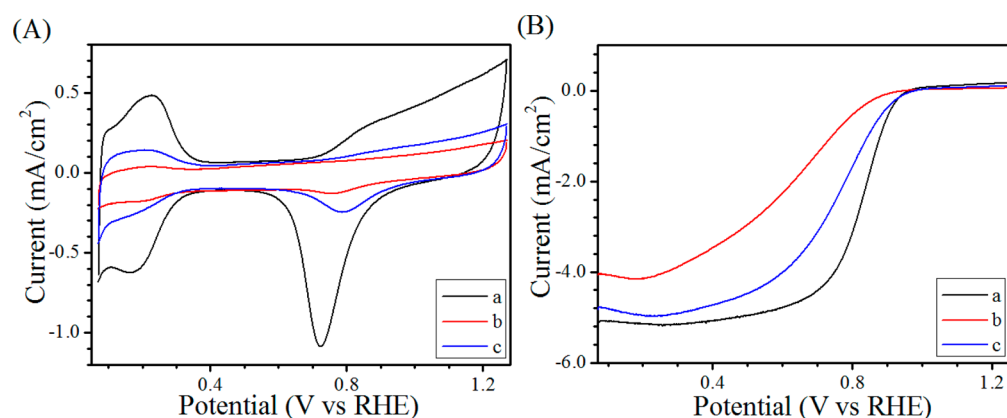
Figure 6. CV (A) and RDE (B) curves for Pt_nPd_{100-n}/C (n = 14 (a, black), 47 (b, red), 64 (c, blue)) catalyst. Electrode: glassy carbon (0.196 cm^2) inked with 10 μg catalysts. Electrolyte: 0.1 M HClO$_4$ saturated with N$_2$ for CV and saturated with O$_2$ for RDE. Scan rate: 50 mV/s (CV) and 10 mV/s and 1600 rpm (RDE).

evident that the lattice parameter increases with atomic ratio of Pt in the nanoparticles, which is consistent with the lattice constant in Figure 4. There is a linear trend of the lattice parameters for different Pt/Pd ratios of PtPd nanoalloy (also see Figure S1, Supporting Information). The fact that the slope differs somewhat from Vegard's law, which applies very well for bulk materials, reflects the structural distortion in the alloy nanoparticles, which is common in nanoparticles due to finite size and surface relaxation effect. The lattice parameters for $Pt_{14}Pd_{86}$ and $Pt_{64}Pd_{36}$ are quite close to the bulk Pd and Pt, respectively. In other words, there is a lattice shrinking for low-Pt nanoalloys and lattice expansion for high-Pt nanoalloys.

3.3. Electrocatalytic Activity for Oxygen Reduction Reaction. The carbon-supported Pt_nPd_{100-n} (n = 14, 47, 64) catalysts were examined by electrochemical measurements for assessing their electrocatalytic activity for ORR. A typical set of CV and RDE data is shown in Figure 5 for Pt_nPd_{100-n} (n = 14, 47 and 64) catalysts. For the CV curves in Figure 6A, $Pt_{14}Pd_{86}/$C catalyst exhibits the largest hydrogen adsorption (−0.2−0.1 V) and Pd-oxide reduction peaks (0.6−0.9 V), indicative of the largest electrochemical active area (ECA), which is in units of m^2/g$_{Pt+Pd}$ (see Figure S3 and Table S2, Supporting Information). Meanwhile, the comparison of RDE curves in O$_2$-saturated 0.1 M HClO$_4$ solution (Figure 6B) shows a clear difference in the kinetic region of ORR with respect to the composition of the catalysts as well as the metal loading. While there were differences in metal loading on the electrode surface for the three PtPd nanoalloys, the changes of the kinetic currents with the composition of the catalysts are translated to changes in mass activity and specific activity by Koutecky−Levich equation in order to compare their electrocatalytic activities.

Figure 7 shows the data of mass activity and specific activity for Pt_nPd_{100-n}/C (n = 14, 47, 64) catalysts as well as commercial Pd/C and Pt/C catalysts, which were obtained from the kinetic current at 0.85 V vs RHE (see values in Table S2, Supporting Information). Apparently, a minimum value was observed at n ∼ 50% Pt for both mass activity and specific activity. Instead, relatively large mass activity and specific activity were observed for $Pt_{14}Pd_{86}/C$ and $Pt_{64}Pd_{36}/C$, exhibiting two maxima of activity as a function of the bimetallic composition. Particularly, for the composition with a very low Pt% in the alloy (i.e., $Pt_{14}Pd_{86}/C$), a mass activity higher than those of the other alloy compositions is evident. Note that the mass activity data were
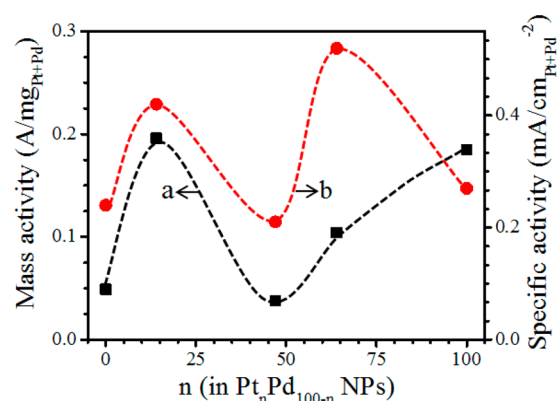

Figure 7. Comparison of mass activity (a) and specific activity (b) at 0.85 V for Pt_nPd_{100-n}/C (n = 0, 14, 47, 64, 100) catalysts. Electrode: Glassy carbon (0.196 cm^2) inked with 10 μg catalysts. Electrolyte: 0.1 M HClO$_4$.

obtained without IR-drop compensation, which is known to increase the values of mass activity and specific activity. Since IR-drop compensation depends on the actual measurement methods, the possible variations could complicate the comparison with most of the literature works.

The electronic properties of Pt and Pd atoms in the nanoalloys were further analyzed using XPS, as shown in Figure 8A. The binding energies of Pt 4f atom in Pt_nPd_{100-n}/C nanoparticles were also analyzed.

The Pt 4f peaks are found to shift slightly to a lower binding energy, showing a minimum for $Pt_{47}Pd_{53}/C$, and then shift to a higher binding energy as Pt is increased in the nanoalloy (Figure 8B). While the values of electronegativity are very similar between Pd (2.20) and Pt (2.28), the shifts of the binding energy suggest that there is subtle electron transfer from Pd to Pt when Pt% increases to ∼50% in the alloy, and there is an electron transfer from Pt to Pd when the alloy is Pt rich.

To the best of our knowledge, this high mass activity at such a low Pt content in the bimetallic catalysts appears entirely new for ORR. We note that a similar finding was reported in a previous study of electrocatalytic oxidation of formic acid over PtPd/C catalysts, where $Pd_{0.9}Pt_{0.1}/C$ was found to be the optimum catalyst among their Pd_xPt_{1-x}/C (x = 0.5−1) samples.[37] However, the origin for the catalytic synergy
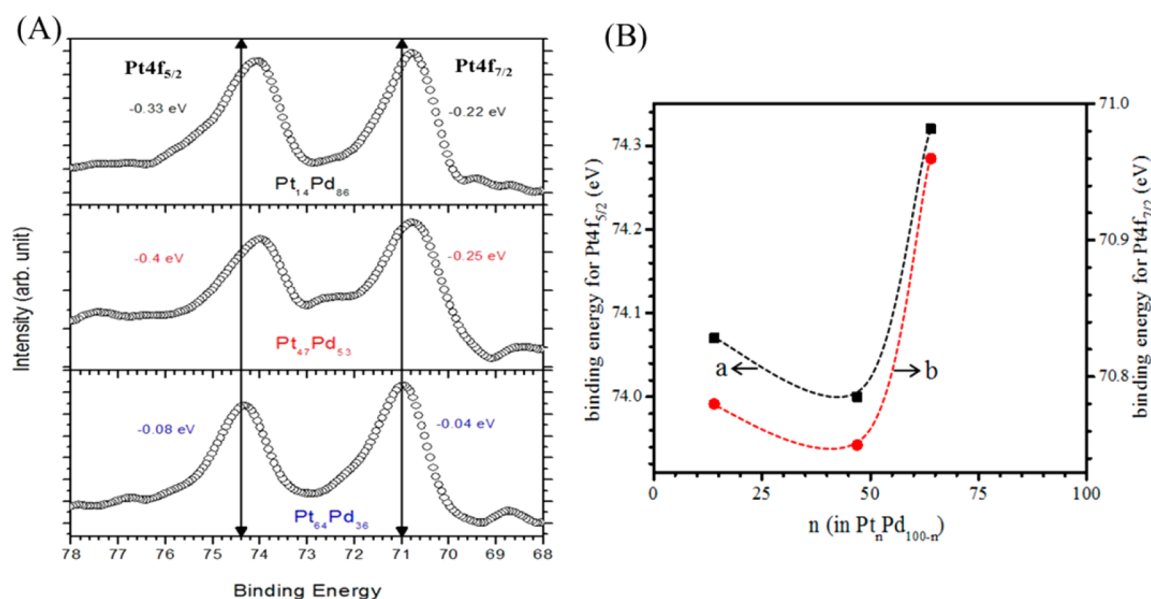
Figure 8. (A)XPS spectra in the Pt 4f binding energy range and the shift value of its peaks, and (B) plots of the peak position of Pt 4f $_{5/2}$ (a) and Pt 4f $_{7/2}$ (b) vs composition for Pt$_n$Pd$_{100-n}$/C (n = 14, 47, 64) catalysts.
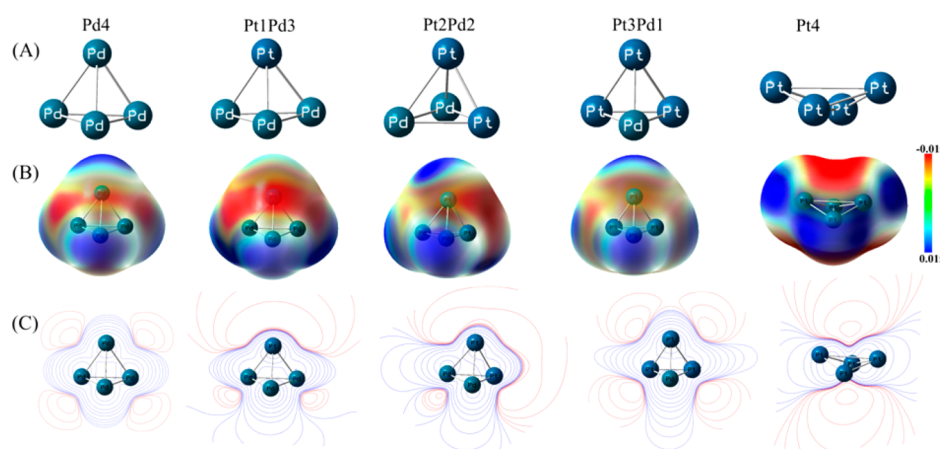

Figure 9. (A) Optimized geometric structure (B) isosurface map and (C) contour map of electrostatic surface potential (ESP) of Pt$_x$Pd$_{4-x}$ (x = 0, 1, 2, 3, 4) clusters by DFT calculation. The calculations used Gaussian 09 and GaussView 5.0, with a model of 4-atom Pt−Pd cluster, involving Optimization; Method via B3LYP functional with LanL2DZ basis set was used to obtain electronic properties and molecular orbitals.

remains elusive, which is further assessed by theoretical modeling based on DFT calculation.

3.4. DFT Calculation. The results of our DFT calculations are discussed in terms of the electronic properties and molecular orbital analysis, and the OH adsorption on the PtPd surface, as detailed below.

3.4.a. Electronic Properties and Molecular Orbital Analysis. In order to understand the correlation between structure and catalytic activity in PtPd bimetallic catalysts, small and basic models of Pt$_x$Pd$_{4-x}$ (x = 0, 1, 2, 3, 4) clusters were chosen for the DFT calculation (using Gaussian 09 software), aiming at providing insights in terms of the electronic properties in comparison with the experimental compositions of the bimetallic nanoparticles.

Figure 9 shows a set of the optimized geometric structures (Figure 9A) and electrostatic surface potential (ESP) of Pt$_x$Pd$_{4-x}$ (x = 0, 1, 2, 3, 4) clusters. The negative region (red) of the ESP corresponds to the nucleophilic reactivity, which could offer adsorption sites for oxygen molecules, while the positive region (blue) is related to the electrophilic reactivity.[38]

As it can been seen from the isosurface map (Figure 9B) and contour map (Figure 9C) of ESP, the red and blue regions distribute uniformly around four atoms for Pd$_4$, Pt$_3$Pd$_1$ and Pt$_4$ clusters, which means these clusters are chemically stable. In the red region in terms of the electron density, there is an enrichment localized around Pt atoms in the Pt$_1$Pd$_3$ and Pt$_2$Pd$_2$ clusters, indicating that Pt atoms in these clusters are active sites for oxygen adsorption by donating electrons to oxygen atom (There is an electron transfer from Pt atom in the clusters to O atom during the adsorption process). The electron transfer between Pt and Pd atoms in Pt$_x$Pd$_{4-x}$ (x = 0, 1, 2, 3, 4) clusters is shown by the natural population analysis in Table S3. It is interesting to note that Pt$_1$Pd$_3$ is more active to adsorb oxygen because the electron density of Pt$_1$Pd$_3$ is larger than that of Pt$_2$Pd$_2$. In contrast, the relative distribution of negative and positive regions of ESP for Pt$_3$Pd$_1$ is rather uniform, suggesting that the active site in Pt$_3$Pd cluster is dispersed around both Pt and Pd atoms.

Considering that electrons transfer occurs from clusters to O atom during the adsorption process, the bonding of O with the
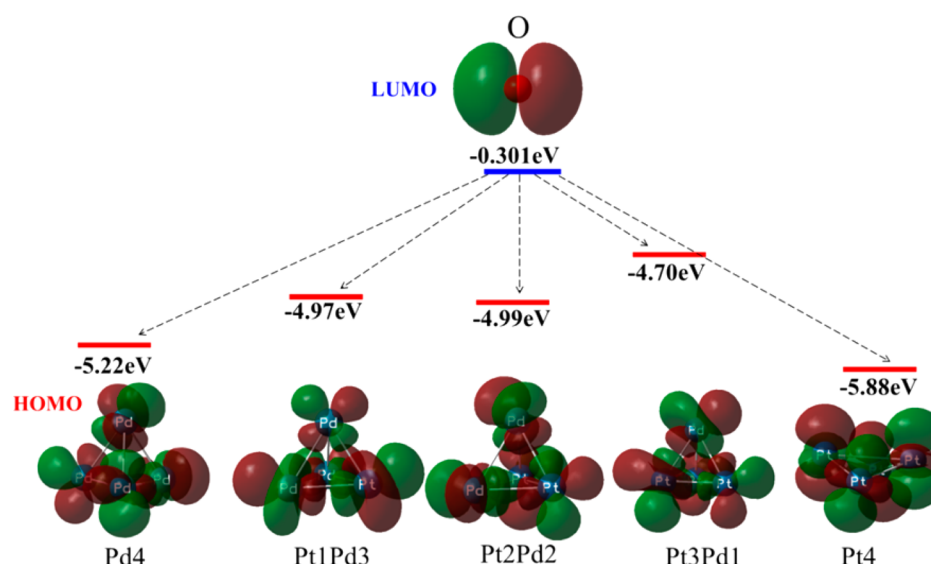
Figure 10. Frontier molecular orbitals, and the energy of LUMO of O atom and HOMO of Pt_xPd_{4-x} (x = 0, 1, 2, 3, 4) clusters.
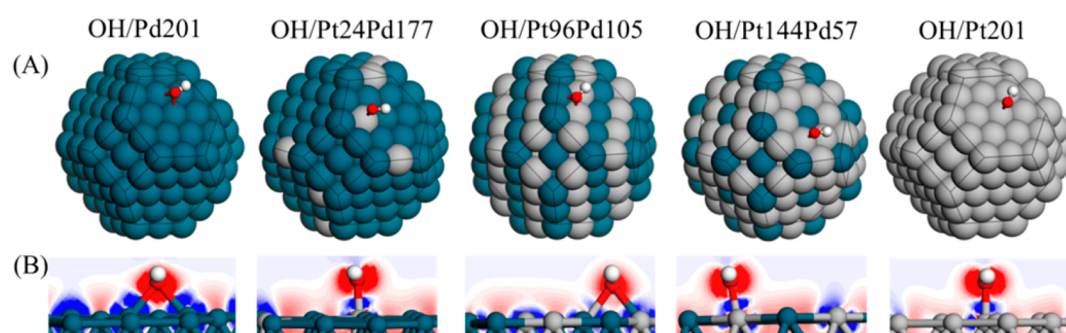

Figure 11. (A) Models of the stable adsorption configurations of OH adsorption, and (B) their deformation electron density on the surface of Pt_xPd_{201-x} (x = 0, 24, 96, 144, 201) clusters. The calculations used DMol3 program of Materials Studio, with a model of 201-atom Pt–Pd cluster in supercell ($6 \times 6 \times 6$ cubic) to enlarge the cell to obtain tetrakaidecahedron, involving first Optimization and then Energy Methods via generalized gradient approximation (GGA) with Perdew–Burke–Ernzerh (PBE) exchange correlation functional, localized double numerical basis sets with polarization functions (DNP) and constraints all atoms. Also, the model puts oxygen molecule on the 201-atom Pt–Pd model surface, followed by Optimization and then Energy methods (color code: Pt in gray, Pd in blue, O in red, and H in white).

nanocluster is further analyzed in terms of the frontier molecular orbitals. The highest occupied molecular orbital (HOMO) of Pt_xPd_{4-x} (x = 0, 1, 2, 3, 4) clusters and the lowest unoccupied molecular orbital (LUMO) of O atom are shown in Figure 10. According to the frontier molecular orbital theory, the reaction of two molecules depends on an interaction between HOMO of one molecule and LUMO of the other one, which depends on the energy difference (ΔE) between HOMO (LUMO) of one molecule and LUMO (HOMO) of the other. Specifically, these clusters have similar HOMO mainly consisting of δ antibonding, thus they have similar interactions with O to form adsorption complexes. The energy difference, $\Delta E = E(\text{LUMO, O}) - E(\text{HOMO}, Pt_xPd_{4-x})$, for Pt_1Pd_3 and Pt_3Pd_1 is relatively small, indicating that the adsorption and desorption of O atom on Pt_1Pd_3 and Pt_3Pd_1 (corresponding to $Pt_{14}Pd_{86}$ and $Pt_{64}Pd_{36}$, respectively) are more favorable than the others including Pt_2Pd_2, Pt_4, and Pd_4. This difference provides some useful information to understand why $Pt_{47}Pd_{53}$ has lowest catalytic activity than $Pt_{14}Pd_{86}$ and $Pt_{64}Pd_{36}$ catalysts.

3.4.b. OH Adsorption on the PtPd (111) Surface. One of the reasons responsible for the sluggish ORR kinetics is the reduction of active sites for O_2 adsorption caused by coverage of OH intermediate during the ORR.[39] Considering that (111)

facets are dominant on the PtPd nanoparticles studied in this work, and the (111) surface is preferable for the fcc structure,[36] we investigated the adsorption energy of OH on PtPd (111) surface model. A more realistic model for the Pt_xPd_{201-x} (x = 0, 24, 96, 144, 201) clusters, corresponding to the composition of Pt_nPd_{100-n}/C (n = 0, 14, 47, 64, 100) catalysts, is established for the analysis of the adsorption of OH on PtPd (111) surface (using Materials Studio software).

Figure 11A shows a set of the stable adsorption configurations of OH on the PtPd (111) surface. Values of the adsorption energy are reported in Table 1. By comparison, the adsorption configurations of O_2 on PtPd (111) surface are also analyzed (see Figure S4 and Table S4, Supporting Information). It can be seen that the adsorption site for O atom of OH on the Pd_{201} and $Pt_{96}Pd_{105}$ clusters features a bridge site, while those on $Pt_{24}Pd_{177}$, $Pt_{144}Pd_{57}$, and Pt_{201}

Table 1. Values of Adsorption Energy (eV) for OH on Pt_xPd_{201-x} (x = 0, 24, 96, 144, 201) Clusters

	Pt_{201}	$Pt_{144}Pd_{57}$	$Pt_{96}Pd_{105}$	$Pt_{24}Pd_{177}$	Pd_{201}
OH	−1.59	−1.67	−1.85	−1.80	−1.82

clusters feature top site. This result indicates that the adsorption strengths on Pd_{201} and $Pt_{96}Pd_{105}$ clusters are stronger than those on $Pt_{24}Pd_{177}$, $Pt_{144}Pd_{57}$, and Pt_{201} clusters. In other words, desorption of the O atom from Pd_{201} and $Pt_{96}Pd_{105}$ clusters would be more difficult, resulting in a decrease of the catalytic activity (see Figure 7).

The deformation electron density for the most stable adsorption structure is shown in Figure 11B. In deformation electron density,[40] the electron density is accumulated around atoms (indicated by the red area), and depleted around atoms (indicated by the blue area). Clearly, O atom of OH (located in the red area) receives electrons, whereas Pt or Pd atoms connected to O (in blue area) lose electrons. This finding reveals that some electrons move from Pd and Pt atoms to O atoms, forming the O−Pd and O−Pt species.

Figure 12 shows a plot of the OH adsorption energies vs concentration of Pt in PtPd alloy clusters. This result exhibits a
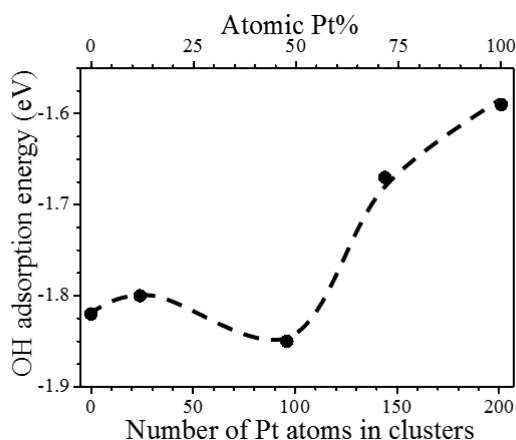

Figure 12. Plot of OH adsorption energy with concentration of Pt in Pt_xPd_{201-x} ($x = 0, 24, 96, 144, 201$) clusters.

trend similar to that observed for the mass activity as a function of the bimetallic composition in the nanoparticles (see Figure 7), reflecting an important role played by the OH intermediate species on the nanoalloy catalysts.

There is a valley appearing at a Pt:Pd ratio of about 50:50. The OH adsorption is thermodynamically favored on that alloy composition in comparison to other compositions. However, the OH formation on PtPd alloys is an important step during ORR, and the high coverage of OH species on the Pt or Pd sites block the Pt or Pd sites for O_2 reduction. The latter may be the reason for the low catalytic activity for that alloy composition.

4. CONCLUSION

In conclusion, Pt_nPd_{100-n}/C catalysts prepared in this work were shown to exhibit fcc-type alloy structure with the lattice parameters shrinking or expanding depending on the bimetallic composition. With nanoalloys of different compositions, $Pd_{47}Pt_{53}$ is shown to exhibit the lowest ORR activity, whereas the low-Pt nanoalloy, $Pd_{14}Pt_{86}$, is shown to display the highest mass activity. The finding of preparing the PtPd catalysts with significantly reduced loading of Pt but high activity is intriguing. With the help of the DFT calculation, the results indicate that Pt atoms in PtPd clusters are active sites for oxygen adsorption by donating electrons to oxygen. The low-Pt nanoclusters are more active to adsorb oxygen because its electron density is

larger than that of the high-Pt clusters. This finding is supported by XPS data showing a subtle electron transfer from Pd to Pt for Pd-rich nanoalloy, and from Pt to Pd for Pt-rich nanoalloy. It is the formation of OH intermediate species which has played an important role during ORR by reducing the coverage of OH-species on the active sites for the low-Pt nanoalloys, which correlates well with the experimental results in terms of the mass activity. These findings have implications for the design of composition-tunable nanoalloy catalysts for ORR.

■ ASSOCIATED CONTENT

⑤ Supporting Information

The Supporting Information is available free of charge on the ACS Publications website at DOI: 10.1021/acs.jpcc.7b03043.

Additional experimental and computational data (PDF)

■ AUTHOR INFORMATION

Corresponding Authors
*(C.J.Z.) E-mail: cjzhong@binghamton.edu.
*(V.P.) E-mail: petko1vg@cmich.edu.
ORCID ⬤
Valeri Petkov: 0000-0002-6392-7589
Chuan-Jian Zhong: 0000-0003-0746-250X
Notes
The authors declare no competing financial interest.

■ ACKNOWLEDGMENTS

■ REFERENCES

(1) Salgado, J. R. C.; Antolini, E.; Gonzalez, E. R. Structure and Activity of Carbon-Supported Pt-Co Electrocatalysts for Oxygen Reduction. *J. Phys. Chem. B* **2004**, *108*, 17767−17774.

(2) Xiong, L.; Manthiram, A. Effect of Atomic Ordering on the Catalytic Activity of Carbon Supported PtM (M= Fe, Co, Ni, and Cu) Alloys for Oxygen Reduction in PEMFCs. *J. Electrochem. Soc.* **2005**, *152*, A697−A703.

(3) Pech-Pech, I. E.; Gervasio, D. F.; Pérez-Robles, J. F. Nanoparticles of Ag with a Pt and Pd Rich Surface Supported on Carbon as a New Catalyst for the Oxygen Electroreduction Reaction (ORR) in Acid Electrolytes: Part 2. *J. Power Sources* **2015**, *276*, 374−381.

(4) Lu, Y. Z.; Jiang, Y. Y.; Chen, W. PtPd Porous Nanorods with Enhanced Electrocatalytic Activity and Durability for Oxygen Reduction Reaction. *Nano Energy* **2013**, *2*, 836−844.

(5) Gupta, G.; Slanac, D. A.; Kumar, P.; Wiggins-Camacho, J. D.; Wang, X. Q.; Swinnea, S.; More, K. L.; Dai, S.; Stevenson, K. J.; Johnston, K. P. Highly Stable and Active Pt-Cu Oxygen Reduction Electrocatalysts Based on Mesoporous Graphitic Carbon Supports. *Chem. Mater.* **2009**, *21*, 4515−4526.

(6) Duan, H. M.; Xu, C. X. Nanoporous PtPd Alloy Electrocatalysts with High Activity and Stability toward Oxygen Reduction Reaction. *Electrochim. Acta* **2015**, *152*, 417−424.

(7) Quan, X. C.; Mei, Y.; Xu, H. D.; Sun, B.; Zhang, X. Optimization of Pt-Pd Alloy Catalyst and Supporting Materials for Oxygen

Reduction in Air-Cathode Microbial Fuel Cells. *Electrochim. Acta* **2015**, *165*, 72−77.

(8) Singh, R. K.; Rahul, R.; Neergat, M. Phys. Stability Issues in Pd-based Catalysts: the Role of Surface Pt in Improving the Stability and Oxygen Reduction Reaction (ORR) Cctivity. *Phys. Chem. Chem. Phys.* **2013**, *15*, 13044−13051.

(9) Jung, D.; Beak, S.; Nahm, K. S.; Kim, P. Enhancement of Oxygen Reduction Activity by Sequential Impregnation of Pt and Pd on Carbon Support. *Korean J. Chem. Eng.* **2010**, *27*, 1689−1694.

(10) Thanasilp, S.; Hunsom, M. Effect of Pt: Pd Atomic Ratio in Pt-Pd/C Electrocatalyst-Coated Membrane on the Electrocatalytic Activity of ORR in PEM Fuel Cells. *Renewable Energy* **2011**, *36*, 1795−1801.

(11) Cheng, D. J.; Wang, W. C. Tailoring of Pd−Pt Bimetallic Clusters with High Stability for Oxygen Reduction Reaction. *Nanoscale* **2012**, *4*, 2408−2415.

(12) Li, H. Q.; Sun, G. Q.; Li, N.; Sun, S.; Su, D. S.; Xin, Q. Design and Preparation of Highly Active Pt-Pd/C Catalyst for the Oxygen Reduction Reaction. *J. Phys. Chem. C* **2007**, *111*, 5605−5617.

(13) Koenigsmann, C.; Santulli, A. C.; Gong, K.; Vukmirovic, M. B.; Zhou, W. P.; Sutter, E.; Wong, S. S.; Adzic, R. R. Enhanced Electrocatalytic Performance of Processed, Ultrathin, Supported Pd-Pt Core−Shell Nanowire Catalysts for the Oxygen Reduction Reaction. *J. Am. Chem. Soc.* **2011**, *133*, 9783−9795.

(14) Jukk, K.; Kongi, N.; Tammeveski, K.; Solla-Gullón, J.; Feliu, J. M. PdPt Alloy Nanocubes as Electrocatalysts for Oxygen Reduction Reaction in Acid Media. *Electrochem. Commun.* **2015**, *56*, 11−15.

(15) Guo, S.; Dong, S.; Wang, E. Ultralong Pt-on-Pd Bimetallic Nanowires with Nanoporous Surface: Nanodendritic Structure for Enhanced Electrocatalytic Activity. *Chem. Commun.* **2010**, *46*, 1869−1871.

(16) Sun, S.; Zhang, G.; Geng, D.; Chen, Y.; Li, R.; Cai, M.; Sun, X. A Highly Durable Platinum, Nanocatalyst for Proton Exchange Membrane Fuel Cells: Multiarmed Starlike Nanowire Single Crystal. *Angew. Chem.* **2011**, *123*, 442−446.

(17) Wang, Q.; Li, Y. J.; Liu, B. C.; Xu, G. R.; Zhang, G.; Zhao, Q.; Zhang, J. A Facile Reflux Procedure to Increase Active Surface Sites Form Highly Active and Durable Supported Palladium@Platinum Bimetallic Nanodendrites. *J. Power Sources* **2015**, *297*, 59−67.

(18) Lv, J. J.; Zheng, J. N.; Wang, Y. Y.; Wang, A. J.; Chen, L. L.; Feng, J. J. A Simple One-Pot Strategy to Platinumepalladium@ Palladium Core-Shell Nanostructures with High Electrocatalytic Activity. *J. Power Sources* **2014**, *265*, 231−238.

(19) Inoue, H.; Sakai, R.; Kuwahara, T.; Chiku, M.; Higuchi, E. Simple Preparation of Pd Core Nanoparticles for Pd Core/Pt Shell Catalyst and Evaluation of Activity and Durability for Oxygen Reduction Reaction. *Catalysts* **2015**, *5*, 1375−1387.

(20) Zhang, G.; Shao, Z. G.; Lu, W. T.; Xie, F.; Qin, X. P.; Yi, B. L. Electrochemical Preparation and Characterization of PdPt Nanocages with Improved Electrocatalytic Activity toward Oxygen Reduction Reaction. *Electrochim. Acta* **2013**, *103*, 66−76.

(21) Wu, J. F.; Shan, S. Y.; Luo, J.; Joseph, P.; Petkov, V.; Zhong, C. J. PdCu Nanoalloy Electrocatalysts in Oxygen Reduction Reaction: Role of Composition and Phase State in Catalytic Synergy. *ACS Appl. Mater. Interfaces* **2015**, *7*, 25906−25913.

(22) Wu, D. F.; Xu, H. X.; Cao, D.; Fisher, A.; Gao, Y.; Cheng, D. J. PdCu Alloy Nanoparticle-Decorated Copper Nanotubes as Enhanced Electrocatalysts: DFT Prediction Validated by Experiment. *Nanotechnology* **2016**, *27*, 495403−495414.

(23) Shan, S. Y.; Petkov, V.; Yang, L. F.; Mott, D.; Wanjala, B. N.; Cai, F.; Chen, B. H.; Luo, J.; Zhong, C. J. Oxophilicity and Structural Integrity in Maneuvering Surface Oxygenated Species on Nanoalloys for CO Oxidation. *ACS Catal.* **2013**, *3*, 3075−3085.

(24) Wu, J. F.; Shan, S. Y.; Petkov, V.; Prasai, B.; Cronk, H.; Joseph, P.; Luo, J.; Zhong, C. J. Composition-Structure-Activity Relationships for Palladium-Alloyed Nanocatalysts in Oxygen Reduction Reaction: An Ex-Situ/In-Situ High Energy X-ray Diffraction Study. *ACS Catal.* **2015**, *5*, 5317−5327.

(25) Petkov, V. Nanostructure by High-Energy X-Ray Diffraction. *Mater. Today* **2008**, *11*, 28−38.

(26) Egami, T.; Billinge, S. J. L. *Underneath the Braggs Peak: Structural Analysis of Complex Materials*. Pergamon: Amsterdam, 2003.

(27) Oxford, S. M.; Lee, P. L.; Chupas, P. J.; Chapman, K. W.; Kung, M. C.; Kung, H. H. Study of Supported PtCu and PdAu Bimetallic Nanoparticles Using In-Situ X-ray Tools. *J. Phys. Chem. C* **2010**, *114*, 17085−17091.

(28) Lian, X.; Tian, W. Q.; Guo, W. L.; Liu, F. L.; Xiao, P.; Zhang, Y. H. DFT Study of Pt$_{7-x}$Ru$_x$ (x = 0, 1, 2, 3) Clusters and their Interactions with CO. *Eur. Phys. J. D* **2014**, *68*, 72−80.

(29) Lian, X.; Guo, W. L.; Liu, F. L.; Yang, Y.; Xiao, P.; Zhang, Y. H.; Tian, W. Q. DFT Studies on Pt3M (M = Pt, Ni, Mo, Ru, Pd, Rh) Clusters for CO Oxidation. *Comput. Mater. Sci.* **2015**, *96*, 237−245.

(30) Xu, Z. F.; Wang, Y. X. Effects of Alloyed Metal on the Catalysis Activity of Pt for Ethanol Partial Oxidation: Adsorption and Dehydrogenation on Pt3M (M = Pt, Ru, Sn, Re, Rh, and Pd). *J. Phys. Chem. C* **2011**, *115*, 20565−20571.

(31) Özcan, M.; Toffoli, D.; Üstünel, H.; Dehri, İ. Insights into Surface−Adsorbate Interactions in Corrosion Inhibition Processes at the Molecular Level. *Corros. Sci.* **2014**, *80*, 482−486.

(32) Xia, M. R.; Ding, W.; Xiong, K.; Li, L.; Qi, X. Q.; Chen, S. G.; Hu, B. S.; Wei, Z. D. Anchoring Effect of Exfoliated-Montmorillonite-Supported Pd Catalyst for the Oxygen Reduction Reaction. *J. Phys. Chem. C* **2013**, *117*, 10581−10588.

(33) Chang, C. R.; Wang, Y. G.; Li, J. Theoretical Investigations of the Catalytic Role of Water in Propene Epoxidation on Gold Nanoclusters: A Hydroperoxyl-Mediated Pathway. *Nano Res.* **2011**, *4*, 131−142.

(34) Tang, W. J.; Zhang, L.; Henkelman, G. J. Catalytic Activity of Pd/Cu Random Alloy Nanoparticles for Oxygen Reduction. *J. Phys. Chem. Lett.* **2011**, *2*, 1328−1331.

(35) Feng, L. Y.; Liu, Y. J.; Zhao, J. X. Iron-Embedded Boron Nitride Nanosheet as a Promising Electrocatalyst for the Oxygen Reduction Reaction (ORR): A Density Functional Theory (DFT) study. *J. Power Sources* **2015**, *287*, 431−438.

(36) Sha, Y.; Yu, T. H.; Merinov, B. V.; Goddard, W. A., III DFT Prediction of Oxygen Reduction Reaction on Palladium-Copper Alloy Surfaces. *ACS Catal.* **2014**, *4*, 1189−1197.

(37) Zhang, H. X.; Wang, C.; Wang, J. Y.; Zhai, J. J.; Cai, W. B. Carbon-Supported Pd-Pt Nanoalloy with Low Pt Content and Superior Catalysis for Formic Acid Electro-oxidation. *J. Phys. Chem. C* **2010**, *114*, 6446−6451.

(38) Ren, X. L.; Xu, S. Y.; Chen, S. Y.; Chen, N. X.; Zhang, S. T. Experimental and Theoretical Studies of Triisopropanolamine as an Inhibitor for Aluminum Alloy in 3% NaCl Solution. *RSC Adv.* **2015**, *5*, 101693−101700.

(39) Fouda-Onana, F.; Savadogo, O. Study of O$_2$ and OH Adsorption Energies on Pd═Cu Alloys Surface with a Quantum Chemistry Approach. *Electrochim. Acta* **2009**, *54*, 1769−1776.

(40) Chen, S. H.; Sun, S. Q.; Lian, B. J.; Ma, Y. F.; Yan, Y. G.; Hu, S. Q. The Adsorption and Dissociation of H$_2$S on Cu (100) Surface: A DTF Study. *Surf. Sci.* **2014**, *620*, 51−58.